

Supernova Remnant Candidates Discovered by the SARAO MeerKAT Galactic Plane Survey

L. D. Anderson^{1,2,3}, F. Camilo⁴, Timothy Faerber^{1,3}, M. Bietenholz^{5,6}, C. Bordiu⁷, F. Bufano⁷,
J. O. Chibueze^{8,9,10}, W. D. Cotton^{4,11}, A. Ingallinera⁷, S. Loru⁷, A. Rigby¹², S. Riggi⁷, M. A. Thompson¹²,
C. Trigilio⁷, G. Umana⁷, and G. M. Williams^{12,13}

¹ Department of Physics and Astronomy, West Virginia University, Morgantown WV 26506, USA

² Adjunct Astronomer at the Green Bank Observatory, P.O. Box 2, Green Bank WV 24944, USA

³ Center for Gravitational Waves and Cosmology, West Virginia University, Chestnut Ridge Research Building, Morgantown, WV 26505, USA

⁴ South African Radio Astronomy Observatory, 2 Fir Street, Observatory 7925, South Africa

⁵ SARAO/Hartebeesthoek Radio Astronomy Observatory, PO Box 443, Krugersdorp 1740, South Africa

⁶ Department of Physics and Astronomy, York University, Toronto, M3J 1P3, Ontario, Canada

⁷ INAF – Osservatorio Astrofisico di Catania, Via S. Sofia 78, I-95123 Catania, Italy

⁸ Department of Mathematical Sciences, University of South Africa, Cnr Christian de Wet Rd and Pioneer Avenue, Florida Park, 1709, Roodepoort, South Africa

⁹ Centre for Space Research, Physics Department, North-West University, Potchefstroom 2520, South Africa

¹⁰ Department of Physics and Astronomy, Faculty of Physical Sciences, University of Nigeria, Carver Building, 1 University Road, Nsukka 410001, Nigeria

¹¹ National Radio Astronomy Observatory, 520 Edgemont Road, Charlottesville, VA 22903, USA

¹² School of Physics and Astronomy, University of Leeds, Leeds LS2 9JT, UK

¹³ Department of Physics, Aberystwyth University, Ceredigion, Cymru, SY23 3BZ, UK

September 26, 2024

ABSTRACT

Context. Sensitive radio continuum data could remove the difference between the number of known supernova remnants (SNRs) in the Galaxy compared to that expected, but due to confusion in the Galactic plane, faint SNRs can be challenging to distinguish from brighter H II regions and filamentary radio emission.

Aims. We wish to exploit new SARAO MeerKAT 1.3 GHz Galactic Plane Survey (SMGPS) radio continuum data, which covers $251^\circ \leq \ell \leq 358^\circ$ and $2^\circ \leq b \leq 61^\circ$ at $|b| \leq 1.5^\circ$, to search for SNR candidates in the Milky Way disk.

Methods. We also use MIR data from the Spitzer GLIMPSE, Spitzer MIPS GAL, and WISE surveys to help identify SNR candidates. The identified SNR candidate are sources of extended radio continuum emission that lack MIR counterparts, are not known as H II regions in the WISE Catalog of Galactic H II Regions, and are not known previously as SNRs.

Results. We locate 237 new Galactic SNR candidates in the SMGPS data. We also identify and confirm the expected radio morphology for 201 objects listed in the literature as being SNRs and 130 previously-identified SNR candidates. The known and candidate SNRs have similar spatial distributions and angular sizes.

Conclusions. The SMGPS data allowed us to identify a large population of SNR candidates that can be confirmed as true SNRs using radio polarization measurements or by deriving radio spectral indices. If the 237 candidates are confirmed as true SNRs, it would approximately double the number of known Galactic SNRs in the survey area, alleviating much of the difference between the known and expected populations.

Key words. H II regions – supernova remnants – radio continuum: ISM

1. Introduction

The number of confirmed Galactic SNRs numbers only a few hundred according to the two most authoritative catalogs: that of Green (2022, hereafter “G22”) ¹, which contains 303 SNRs ², and “SNRCat” (Ferrand & Safi-Harb 2012), which lists 383 objects in the online catalog ³. Based on OB star counts, pulsar birth rates, Fe abundances, and the SN rate in other Local Group galaxies, there should

be $\gtrsim 1000$ Galactic SNRs (Li et al. 1991; Tammann et al. 1994). Ranasinghe & Leahy (2022) suggested that there actually may be a few thousand Galactic SNRs based on the population detected to date and on SNR search selection effects. The difference between the identified population of Galactic SNRs and the expected number is likely due to a lack of sensitive radio continuum data and confusion in the Galactic plane (e.g., Brogan et al. 2006; Ranasinghe & Leahy 2022).

The Galactic supernova rate is key to understanding the properties and dynamics of the Milky Way. The number of SNRs in the Galaxy is related to recent massive star formation activity (cf. Tammann et al. 1994). Supernovae

¹ <https://www.mrao.cam.ac.uk/surveys/snr/>

² The most recent published version is that of Green (2014); we use here the version found online.

³ <http://snrcat.physics.umanitoba.ca/>

inject energy into the interstellar medium (ISM), driving molecular cloud turbulence and galactic fountains out of the disk (de Avillez & Breitschwerdt 2005; Joung et al. 2009; Padoan et al. 2016; Girichidis et al. 2016); they therefore affect the disk scale height and star formation properties of a galaxy (Ostriker et al. 2010; Ostriker & Shetty 2011; Faucher-Giguère et al. 2013).

SNRs can be most efficiently identified using radio data. According to our assessment of the G22 catalog, $\sim 90\%$ of known SNRs are detected and well-defined in the radio regime, $\sim 40\%$ detected in X-rays, and $\sim 30\%$ in the optical. More sensitive radio observations may increase the number detected further. The most common radio morphology in the G22 catalog, $\sim 80\%$ of SNRs, is that of a limb-brightened shell or a partial shell, where the diameter of the shell is set by the expanding shock wave produced by the explosion. SNRs can also be classified as “filled-centre” or “plerions,” if they have centrally concentrated radio emission, which is generally caused by a pulsar wind nebula (e.g., the Crab nebula, Weiler & Sramek 1988; Bietenholz et al. 2015), “composite,” for which the SNR appears to have both a shell and an internal component (either a nonthermally-emitting pulsar-driven nebula or a thermally-emitting x-ray source) (see Dubner & Giacani 2015, for a review of radio SNR morphologies).

Separating nonthermally-emitting SNRs from the much more common thermally emitting H II regions in the Galactic plane is challenging. There are $\gtrsim 7000$ identified Galactic H II regions (Armentrout et al. 2021). If there are data at multiple radio frequencies, one can compute the spectral index α , where $S \propto \nu^\alpha$ with S being the flux density and ν the frequency⁴. Most SNRs have spectral indices in the range from $\alpha = -0.8$ to $\alpha = 0.0$, whereas H II regions should have $\alpha \sim -0.1$ if optically thin and $\alpha > -0.1$ if optically thick. Although a spectral index value near 0 does not discriminate between the two classifications, values $\alpha \lesssim -0.2$ indicate nonthermal emission, and therefore an SNR rather than an H II region. The computation of the spectral index, however, is difficult because all radio continuum datasets must have sensitivity to the same spatial scales. Also, filled-center SNRs may have spectral indices near -0.1 (e.g., Bietenholz & Bartel 2008, find $\alpha = 0.08$ for G21.5–0.5). An additional indication of nonthermal emission may come from the presence of polarized radio continuum emission, although due to the fact that the polarized emission fraction is often quite low, this criterion is also difficult to apply (Dokara et al. 2018). In a SNR, the intrinsic polarization angle usually follows the bright ridges of emission (e.g., Cotton et al. 2024), but the presence of polarized emission in the same direction as a SNR does not necessarily mean that it is a SNR.

An easier and perhaps more reliable criterion for separating H II regions from SNRs is the mid-infrared (MIR) to radio continuum flux ratio. Although MIR emission can be detected from SNRs in some cases (Reach et al. 2006; Pinheiro Gonçalves et al. 2011), many researchers have shown that SNRs are deficient in MIR emission compared to H II regions (e.g., Cohen & Green 2001; Pinheiro Gonçalves et al. 2011). The MIR to radio flux ratio for SNRs is about 100 times lower than that of optically thin H II regions.

In the last decade, studies of radio continuum and infrared data have identified a large number of Galactic supernova remnant (SNR) candidates. Those that have been confirmed as SNRs are in the SNR catalogs discussed previously, but the majority are awaiting confirmation. Green et al. (2014) used the anti-correlation between radio and $8\mu\text{m}$ emission to locate 23 new SNR candidates from 843 MHz Molonglo Galactic Plane Survey (MGPS) data. Anderson et al. (2017) used 1.4 GHz continuum data from The HI, OH, Recombination line survey of the Milky Way (THOR; Beuther et al. 2016), combined with the 1.4 GHz radio continuum data from the VLA Galactic Plane Survey (VGPS Stil et al. 2006), to identify 76 new SNR candidates. Dokara et al. (2018) confirmed two of these 76 candidates as true SNRs using spectral index measurements. Hurley-Walker et al. (2019) found 27 new SNRs using data from the GaLactic and Extragalactic All-sky Murchison Wide-field Array (GLEAM) survey and confirmed 26 of them using spectral index measurements; these 26 are listed as known SNRs in G22. Dokara et al. (2021) used data from the 4–8 GHz GLOSTAR survey to identify 157 SNR candidates, 9 of which have nonthermal emission based on polarization measurements. And, finally, Ball et al. (2023) identified 13 new Galactic SNR candidates in 933 MHz Australian Square Kilometre Array Pathfinder (ASKAP) data. These studies followed those of Helfand et al. (2006), which discovered 49 new SNR candidates in The Multi-Array Galactic Plane Imaging Survey (MAGPIS) 20 cm data, and Brogan et al. (2006), which discovered 35 SNR candidates in their VLA data. Even if all the recently-identified SNR candidates are confirmed as true SNRs, there remains a difference between the number of detected Galactic SNRs compared to that expected.

Here, we use new 1.3 GHz SARAO MeerKAT Galactic Plane Survey data (“SMGPS”) to identify SNR candidates in the inner Galaxy. This work complements that of Bordiu et al. (2024, submitted), who used SMGPS data to create an extended source catalog, and Loru et al. (2024, submitted), who provide an in-depth study of 28 Galactic SNRs in SMGPS data for which flux and spectral indices can be derived.

2. Data

2.1. SARAO MeerKAT Galactic Plane Survey (SMGPS)

The ideal radio continuum dataset for SNR searches is sensitive to large, extended structures but also boasts high angular resolution. Extended source sensitivity is necessary for the detection of low surface brightness SNRs and high angular resolution allows one to disentangle the complicated emission of the Galactic plane.

The 1.3 GHz SMGPS (Goedhart et al. 2024)⁵ covers $251^\circ \leq \ell \leq 358^\circ$ and $2^\circ \leq b \leq 61^\circ$ at $|b| \leq 1.5^\circ$. The boundaries at high and low Galactic latitudes are slightly irregular because the survey follows the Galactic warp. A full description of the radio observations and the data reduction procedures is provided in Goedhart et al. (2024). Observations used the 64 antenna MeerKAT array in the Northern Cape Province of South Africa, which is described

⁴ We are using the convention that positive values of α indicate increasing flux densities with frequency.

⁵ Data can be found here: <https://doi.org/10.48479/3wfd-e270>. When using DR1 products, Goedhart et al. (2024) should be cited, and the MeerKAT telescope acknowledgement included.

in Jonas & MeerKAT Team (2016), Camilo et al. (2018), and Mauch et al. (2020). We use here the “zeroth moment” data, which have a central frequency of 1293 MHz with a total used bandwidth of 672 MHz (these values both decrease at high and low Galactic latitudes; see Goedhart et al. 2024). The angular resolution is $\sim 8''$ and the data are sensitive to emission up to angular scales of $\sim 30'$. The background rms noise in areas far from the Galactic Plane and bright point sources is $\sim 30 \mu\text{Jy beam}^{-1}$. The low surface brightness noise threshold together with the sensitivity to both large and small-scale structures makes the SMGPS survey the ideal data set to identify new SNRs.

2.2. MIR data

Over the zone $65^\circ > \ell > -100^\circ$, $|b| < 1.0^\circ$ we use Spitzer 8.0 and $3.6 \mu\text{m}$ data from the GLIMPSE survey (Benjamin et al. 2003; Churchwell et al. 2009) and $24 \mu\text{m}$ data from the MIPS GAL survey (Carey et al. 2009). Outside this zone we use data from the all-sky Widefield Infrared Survey Explorer (WISE; Wright et al. 2010) at 12 and $22 \mu\text{m}$. Since the GLIMPSE and MIPS GAL surveys have better angular resolution and sensitivity than that of WISE, we use Spitzer data when possible.

H II regions have strong emission at these wavelengths. The $\sim 10 \mu\text{m}$ emission is largely from polycyclic aromatic hydrocarbons (PAHs), which fluoresce in the presence of soft ultra-violet ($\sim 5 \text{ eV}$) radiation (Voit 1992) and the $\sim 20 \mu\text{m}$ emission is mainly from small dust grains cospatial with the H II region plasma.

For most SNRs, MIR emission at these wavelengths is largely absent, or at least is at a low intensity compared to that of H II regions (e.g., Cohen & Green 2001; Pinheiro Gonçalves et al. 2011). Some young SNRs do have strong MIR emission, however, especially at $\sim 20 \mu\text{m}$. The origin of this emission is dust, atomic/molecular line emission, or synchrotron emission, with the relative importance of each depending on the SNR in question (see Gonçalves et al. 2011, for a concise summary).

2.3. The WISE Catalog of Galactic H II Regions

The WISE Catalog of Galactic H II Regions (Anderson et al. 2014, hereafter the “WISE Catalog”) is the largest catalog of Galactic H II regions. All catalog entries have WISE (Wright et al. 2010) $\sim 20 \mu\text{m}$ emission surrounded by $\sim 10 \mu\text{m}$ emission (Anderson et al. 2011). The WISE catalog contains ~ 8000 objects with the MIR morphology of H II regions. The $\sim 20 \mu\text{m}$ emission from H II regions is caused by small stochastically heated dust grains that are mixed with the H II region plasma, while the $\sim 10 \mu\text{m}$ intensity is dominated by emission from PAHs. All known Galactic H II regions have this characteristic morphology. Here, we use Version 3.0 of the catalog⁶.

2.4. SNR Catalogs

The G22 catalog currently contains 303 regions compiled from the literature. Green (2004) suggest that a previous (but similar) version of the catalog was largely complete to a radio surface density limit of $10^{-20} \text{ W m}^{-2} \text{ Hz}^{-1} \text{ sr}^{-1}$ (1 MJy sr^{-1}). At the $8''$ resolution of the SMGPS data, this

corresponds to $1.7 \text{ mJy beam}^{-1}$, or ~ 60 times greater than the SMGPS 1σ point source sensitivity. In addition to the surface brightness limit, the catalog appears to be lacking the small angular size SNRs that are expected (Green 2015).

SNRCat (Ferrand & Safi-Harb 2012) contains 383 entries in the most recent online version and focuses largely on their high energy emission. All G22 sources are also included in SNRCat. Even though there are more entries than in G22, many of these are not the same as the SNRs listed in G22; SNRCat includes pulsar wind nebulae, bow-shock nebulae, high-energy (X-ray and gamma-ray) discovered SNRs, and magnetar-hosting SNRs.

As there are significant differences in their compositions, we treat G22 and SNRCat separately. Although both catalogs cover the entire sky, since they are not derived from homogeneous data sets, the catalog sensitivities vary with Galactic location. Both catalogs contain at a minimum spatial coordinates and angular sizes for all entries. When the extent of the SNR is listed with an ellipse, we instead use a circle that has an angular radius that is an average between that of the semimajor and semiminor axes.

2.5. SNR Candidate Catalogs

There are numerous extant catalogs of SNR candidates. We primarily use the compilation of previously-known and newly-discovered SNR candidates in Dokara et al. (2021), which includes results from Brogan et al. (2006); Helfand et al. (2006); Anderson et al. (2017); Hurley-Walker et al. (2019). We supplement this list using the results from numerous other studies compiled in the G22 documentation and additionally add the recent study of Ball et al. (2023). Over the SMGPS range, there are 190 SNR candidates; 74 of these were compiled by Dokara et al. (2021), and 78 were identified for the first time by Dokara et al. (2021).

As with the known SNRs, in cases where the extent of the SNR candidate is defined with an ellipse, we instead use a circle that has a radius in between that of the semimajor and semiminor axes.

3. Method

The present study has two main goals: 1) to assess the radio emission from known and candidate SNRs in the SMGPS data and 2) to identify new SNR candidates.

For the first goal, we inspect SMGPS and MIR data at the positions of all known and candidate SNRs from the catalogs in Sections 2.4 and 2.5. We take the coordinates of a given object from the most recent published study, which is not necessarily the same as that listed in the catalogs. During this visual inspection, we primarily seek to ascertain if the identified SNR or SNR candidate is detected in the SMGPS. If it is, we determine if it is confused with an H II region.

For the second goal, our identification methodology is similar to that used by numerous recent authors (e.g., Anderson et al. 2017; Dokara et al. 2021; Ball et al. 2023): we identify discrete regions of radio continuum emission that 1) have a radio morphology consistent with known SNRs (i.e. roughly circular), 2) are not identified as being H II regions in the WISE Catalog, known SNRs, or SNR candidates, and 3) lack Spitzer or WISE MIR emission charac-

⁶ <http://astro.phys.wvu.edu/wise>

teristic of thermal sources. Criteria #2 and #3 are somewhat redundant, as nearly all discrete sources of coincident MIR and radio continuum emission in the Galactic plane are H II regions and are included in the WISE catalog. As mentioned previously, some SNRs do have MIR emission, but the quality of this emission differs between SNRs and H II regions. Aside from the radio-to-MIR flux ratio being higher for SNRs than for H II regions (e.g., [Cohen & Green 2001](#); [Pinheiro Gonçalves et al. 2011](#)), the $\sim 24\mu\text{m}$ emission for SNRs more closely follows the radio than for H II regions, and there is no related $\sim 10\mu\text{m}$ emission.

We illustrate the by-eye identification process in Figure 1. We first identify the SMGPS emission associated with all known SNRs and SNR candidates (red and green circles, respectively). We then identify all discrete, extended radio continuum sources that are not associated with these SNRs or SNR candidates, and also are not associated with H II regions in the WISE Catalog. We classify such sources as new SNR candidates (light green) or unusual objects (pink). We inspect each SMGPS field on three separate occasions to ensure that we identify as many SNR candidates as possible.

We do not have a preferred morphology for the identified SNR candidates aside from requiring that the emission is relatively circularly symmetric. We then search the MIR data for emission of a complementary morphology to that of the SMGPS data, which allows us to remove any remaining H II regions not included in the WISE Catalog. We classify the remaining radio continuum sources as SNR candidates.

We approximate the center and angular extent of each identified object by defining a circle that encloses its SMGPS emission. Our method therefore defines new positions for all known and candidate SNRs in the SMGPS zone. For partial shells, the defined circle follows the curvature of the shell. Too, if the source is partially off the SMGPS zone, we define the circle following the emission that is detected; such centroids and radii can therefore be quite uncertain.

For each newly-identified SNR candidate, we query the Simbad database⁷, with a search radius of $5'$. This process allows us to remove previously-identified objects from the sample.

4. Results

We summarize the results of our investigation of previously-known SNRs, previously-identified SNR candidates, and newly-discovered sources in Table 1. This table lists for each category the number of objects, and the number confirmed as SNRs or SNR candidates (if previously-known). We give more details on these samples in the following subsections.

Images and SMGPS FITS cutouts for all objects studied are hosted on <https://doi.org/10.48479/On8c-5q84>.

4.1. Previously-Identified SNRs

We detect SMGPS emission from all 187 G22 SNRs whose centroids fall within the SMGPS area. Of these, we confirm 184, listed in Table 2, and show examples in Figure 2. In this table we revise the coordinates and sizes of the SNRs to enclose the SMGPS emission, but use the G22 source names.

⁷ <https://simbad.u-strasbg.fr/simbad/>

Table 1: Summary of Sources Studied

Category	Number	Confirmed
Known SNRs	238	201
G22	187	184
SNRCat (unique) ^a	51	17
Known SNR Candidates	170	130
New SNR Candidates ^b	237	...
Class I	83	...
Class II	104	...
Class III	50	...
Unusual	49	...

Notes. ^(a) “Unique” refers to sources only in SNRCat, but not in G22. ^(b) New SNR candidates are classified from I to III in order of decreasing reliability; see Section 4.3.

Although some known SNRs in the sample do have MIR emission, the quality of this emission is very different from that of H II regions. For example, for SNR G11.2–0.3 shown in Figure 2, there is bright $24\mu\text{m}$ emission. Compared to H II regions, however, this source is lacking the $\sim 10\mu\text{m}$ emission that delineates a photodissociation region. Therefore, one can visually distinguish between SNRs and H II regions, even for those SNRs that are bright at $24\mu\text{m}$.

We separate one G22 source into two SNRs. The G22 source G337–0.1 refers to a small $\sim 1'$ diameter object. The larger shell, which was also called G337–0.1 in previous versions of the G22 catalog, is also detected in SMGPS data; we include the larger shell as a separate catalog entry using the name G337–0.1*. We show these two regions in Figure 3.

We think that two G22 sources are unlikely to be true SNRs. Although the source G298.5–0.3 is unambiguously detected in SMGPS data, it consists of two linear filaments and has a radio morphology inconsistent with the morphology of known SNRs. It fits the criteria for “unusual” sources discussed later and is included there. This source looks like a convincing SNR in low-resolution radio continuum emission from [Whiteoak & Green \(1996\)](#), but the SMGPS data reveals its true morphology. The source G011.8–00.2 overlaps with the WISE Catalog H II region G011.887–00.253. We show these two sources in Figure 4.

We detect SMGPS emission from 30 SNRCat objects that are not in the G22 catalog, out of 51 examined. We list the detected SNRCat objects in Table 3. In this table we revise the coordinates and sizes of the sources to enclose the SMGPS emission, but use the catalog source names.

Of the detected sources, six are compact ($\sim 30''$ or less) pulsar wind nebulae (PWNe; G267.0–1.0, G284.0–1.8, G336.4+0.2, G350.2–0.8, G18.0–0.7, and G36.0+0.1). Two are long, linear PWNe (G319.9–0.7 and G337.5–0.1). Five are listed in SNRCat as being PWNe or candidates, but have extended radio continuum emission (G313.3+0.1, G313.6+0.3, G333.9+00.0, G348.9–0.4, and G29.4+0.1). The remaining 17 sources have radio morphologies similar to the SNRs in G22. Of these 17, 15 are listed in [Green et al. \(2014\)](#) as being SNR candidates.

We suggest that nine of the examined SNRCat sources are not true SNRs. Of these, four overlap with WISE Catalog H II regions: G8.3–0.0 overlaps with G008.306–00.084, G10.5–0.0 overlaps with G010.585–00.051, G11.0–1.0 overlaps with G011.182–01.063, and G14.3+0.1 overlaps

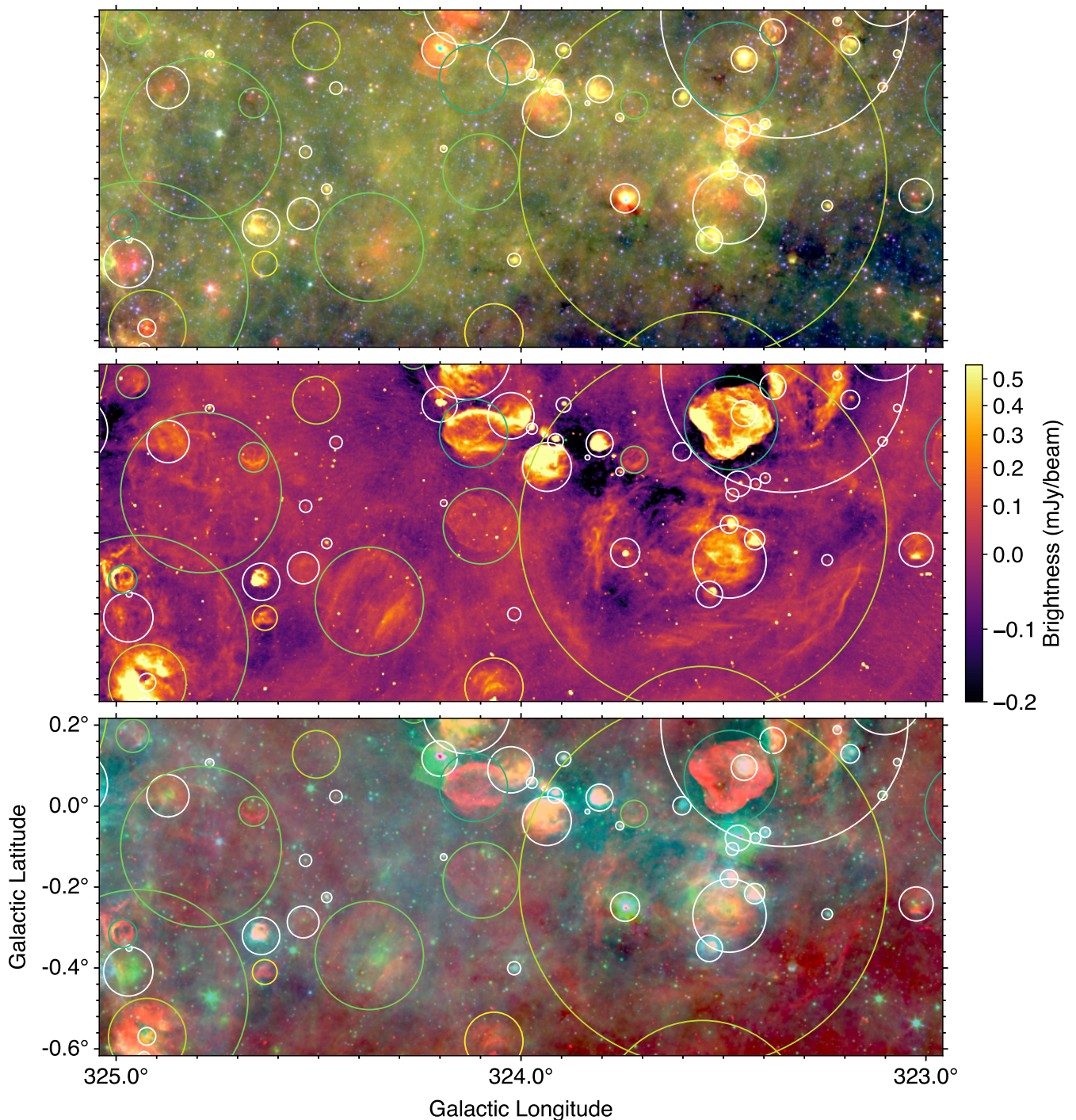


Fig. 1: Example field centered at $(\ell, b) = (324.0^\circ, -0.2^\circ)$. The top panel shows Spitzer three-color data, with MIPSGAL $24\mu\text{m}$ data in red, GLIMPSE $8.0\mu\text{m}$ data in green, and GLIMPSE $3.6\mu\text{m}$ data in blue. The middle panel shows the 1.3 GHz SMGPS images. The bottom panel has 1.3 GHz SMGPS images in red, MIPSGAL $24\mu\text{m}$ data in green and GLIMPSE $8.0\mu\text{m}$ data in blue. White circles show H II regions from the WISE Catalog (Section 2.3), blue-green circles show previously-known SNRs (Section 4.1), green circles show previously-known SNR candidates (Section 4.2), light green circles show SNR candidates newly identified here (Section 4.3), and yellow circles show “Unusual” sources (Section 4.4). Although there are no examples in this field, in subsequent figures we show misidentified or nondetected SNRs and SNR candidates with dashed circles.

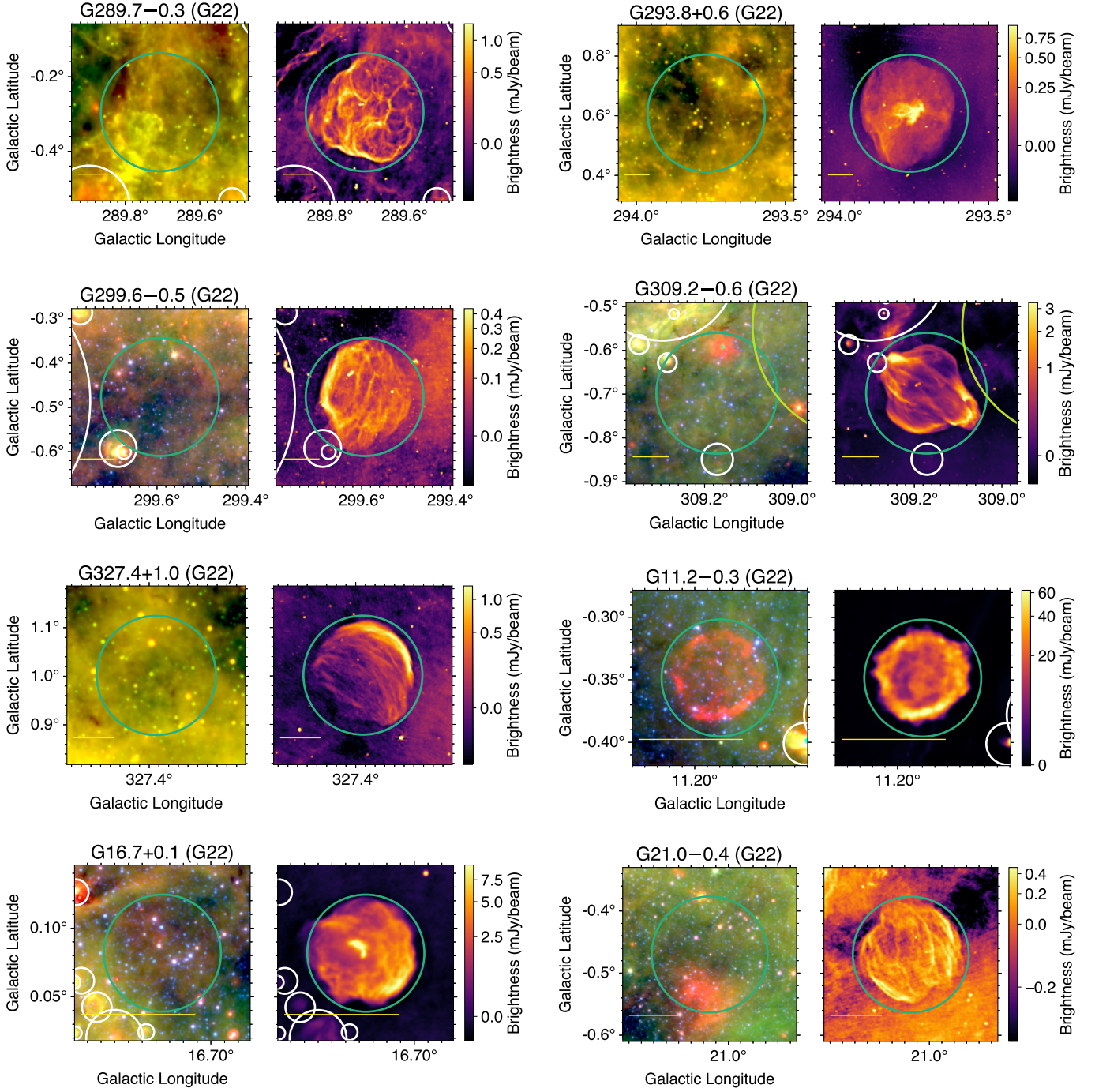


Fig. 2: Objects from the G22 catalog. MIR data is in the left panels (Spitzer or WISE) and SMGPS 1.3 GHz data are on the right. The symbols have the same meaning as in Figure 1, with the G22 SNRs being represented by blue-green circles at the centers of all panels. Cyan scale bars at the lower left of each panel are 5' long.

with G014.303+00.140. The radio emission from one, G354.4+0.0, consists of a broad radio filament and based on their MIR emission four appear to be thermal but are not confused with individual H II regions: G284.2-0.4, G304.1-0.2, G21.9-0.1, and G026.6-0.1.

Additionally, 12 SNRCat sources have no identifiable SMGPS emission: G285.1-00.5, G287.4+00.6, G323.9+00.0, G331.5-00.6, G332.5-00.3, G344.7+00.1, G350.2-00.8, G358.1+00.1, G358.3+00.2, G018.5-00.4, G032.73+0.15, G032.6+00.5, G044.5-00.2. All except for

G331.5-00.6 are listed as being PWNe or candidates, so their lack of SMGPS emission is unsurprising.

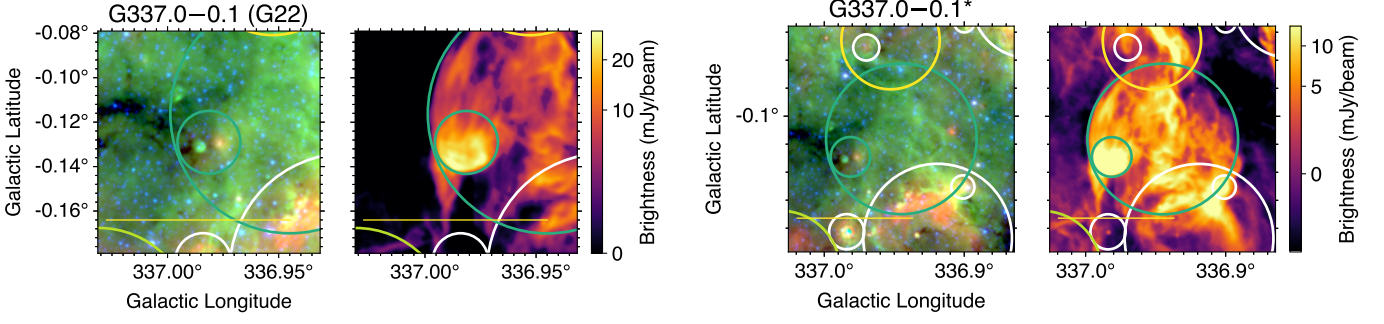


Fig. 3: Objects from the G22 catalog that we split into two entries, G337.0–0.1* (left panels) and G337.0–0.1 (right panels). MIR data is in the left panels and SMGPS 1.3 GHz data are on the right. The symbols have the same meaning as in Figure 1, with the G22 SNRs being represented by blue-green circles at the centers of all panels. Yellow scale bars at the lower left of each panel are 5' long.

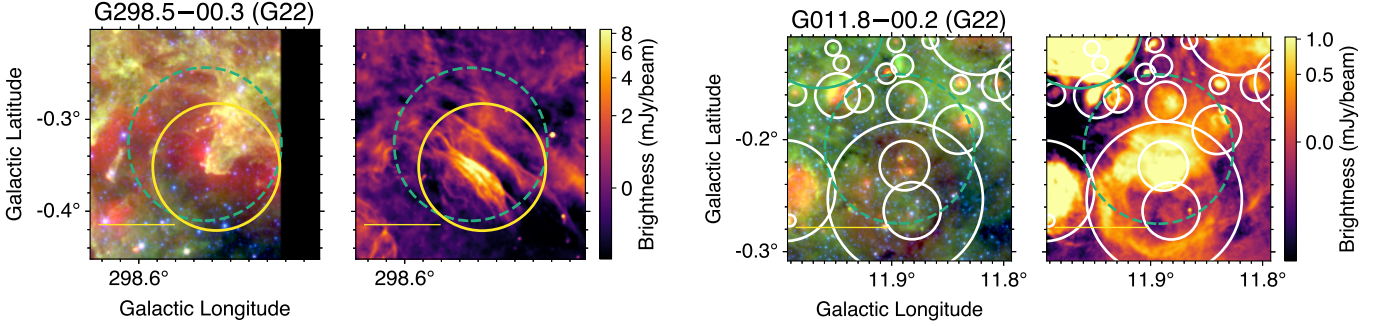


Fig. 4: Objects from the G22 catalog that are unlikely to be true SNRs. MIR data is in the left panels (Spitzer or WISE) and SMGPS 1.3 GHz data are on the right. The symbols have the same meaning as in Figure 1, with the G22 SNRs being indicated by blue-green dashed circles at the centers of all panels. Yellow scale bars at the lower left of each panel are 5' long.

Table 2: Previously-Identified SNRs From G22

Name ^a	GLong deg.	GLat deg.	Radius arcmin.
G266.2–1.2	266.183	–1.193	51.5
G279.0+1.1	278.958	0.761	67.2
G284.3–1.8	284.279	–1.826	17.3
G286.5–1.2	286.217	–1.104	23.2
G289.7–0.3	289.707	–0.295	9.5
G290.1–0.8	290.102	–0.754	9.6
G291.0–0.1	291.033	–0.099	7.5
G292.2–0.5	292.142	–0.532	9.9
G293.8+0.6	293.766	0.608	11.8
G294.1–0.0	294.125	–0.046	21.7
G296.1–0.5	295.929	–0.547	33.1
G296.7–0.9	296.661	–0.922	7.6

Table 2, continued.

Name ^a	GLong ^b deg.	GLat deg.	Radius arcmin.
G296.8–0.3	296.885	–0.350	10.3
G298.6–0.0	298.573	–0.063	6.2
G299.6–0.5	299.593	–0.476	8.0
G301.4–1.0	301.432	–1.006	14.4
G302.3+0.7	302.282	0.717	9.7
G304.6+0.1	304.585	0.126	4.6
G306.3–0.9	306.309	–0.890	2.2
G308.1–0.7	308.122	–0.672	9.2
G308.4–1.4	308.477	–1.373	8.2
G308.8–0.1	308.860	–0.199	8.8
G309.2–0.6	309.172	–0.698	8.3
G309.8+0.0	309.779	0.006	13.6
G310.6–0.3	310.618	–0.283	4.7
G310.8–0.4	310.816	–0.475	5.8
G311.5–0.3	311.524	–0.340	2.4
G312.4–0.4	312.452	–0.423	17.6
G315.4–0.3	315.469	–0.253	12.4
G315.9–0.0	315.895	–0.015	10.0

Table 2, continued.

Name ^a	GLong ^b deg.	GLat deg.	Radius arcmin.
G316.3−0.0	316.272	−0.021	12.9
G317.3−0.2	317.296	−0.258	6.8
G318.2+0.1	318.148	0.161	28.3
G318.9+0.4	318.897	0.411	16.0
G320.4−1.2	320.382	−1.232	18.0
G321.9−0.3	321.913	−0.312	15.9
G321.9−1.1	321.929	−1.069	16.0
G322.1+0.0	322.105	0.023	3.7
G322.5−0.1	322.471	−0.101	8.0
G323.5+0.1	323.481	0.072	6.9
G323.7−1.0	323.591	−1.134	15.3
G326.3−1.8	326.310	−1.714	18.5
G327.1−1.1	327.139	−1.075	10.5
G327.2−0.1	327.239	−0.129	2.9
G327.4+0.4	327.276	0.520	11.4
G327.4+1.0	327.385	1.002	7.4
G328.4+0.2	328.412	0.225	3.3
G329.7+0.4	329.722	0.374	20.2
G330.2+1.0	330.155	0.977	5.5
G332.0+0.2	331.989	0.173	5.9
G332.4+0.1	332.387	0.127	7.3
G332.4−0.4	332.423	−0.373	5.5
G335.2+0.1	335.182	0.109	11.0
G336.7+0.5	336.740	0.540	6.8
G337.0−0.1	336.981	−0.129	0.8
G337.2+0.1	337.184	0.065	1.5
G337.2−0.7	337.210	−0.724	3.1
G337.3+1.0	337.336	0.959	6.6
G337.8−0.1	337.807	−0.094	3.6
G338.1+0.4	338.076	0.424	7.6
G338.3−0.0	338.327	−0.044	4.2
G338.5+0.1	338.535	0.101	3.6
G340.4+0.4	340.405	0.422	4.9
G340.6+0.3	340.586	0.346	2.9
G341.2+0.9	341.116	0.830	14.9
G341.9−0.3	341.846	−0.306	4.2
G342.0−0.2	341.956	−0.200	5.5
G342.1+0.9	342.107	0.888	5.5
G343.1−0.7	343.072	−0.668	12.0
G344.7−0.1	344.682	−0.184	5.1
G345.1−0.2	345.063	−0.204	3.5
G345.1+0.2	345.155	0.244	6.6
G345.7−0.2	345.734	−0.186	3.2
G346.6−0.2	346.611	−0.218	4.9
G347.3−0.5	347.362	−0.582	28.8
G348.5+0.1	348.454	0.094	4.7
G348.5−0.0	348.547	−0.003	5.1
G348.7+0.3	348.646	0.399	5.4
G348.8+1.1	348.860	1.126	6.5

Table 2, continued.

Name ^a	GLong ^b deg.	GLat deg.	Radius arcmin.
G349.2−0.1	349.149	−0.092	4.0
G349.7+0.2	349.728	0.172	1.4
G350.1−0.3	350.065	−0.325	2.7
G351.2+0.1	351.263	0.164	4.8
G351.7+0.8	351.710	0.819	8.1
G351.9−0.9	351.926	−0.959	6.9
G352.7−0.1	352.744	−0.125	4.1
G353.3−1.1	353.514	−1.213	21.5
G353.6−0.7	353.541	−0.670	16.7
G354.1+0.1	354.166	0.053	4.5
G354.8−0.8	354.864	−0.764	10.3
G355.4+0.7	355.345	0.627	24.0
G355.6−0.0	355.675	−0.078	3.9
G356.3−0.3	356.312	−0.357	5.2
G356.3−1.5	356.322	−1.535	10.1
G357.7+0.3	357.706	0.324	13.8
G357.7−0.1	357.714	−0.112	9.7
G358.1+1.0	358.119	1.052	12.1
G1.4−0.1	1.448	−0.148	5.6
G1.9+0.3	1.871	0.323	0.9
G3.1−0.6	3.061	−0.691	28.0
G3.7−0.2	3.779	−0.288	7.0
G3.8+0.3	3.860	0.393	10.9
G5.4−1.2	5.378	−1.222	18.6
G5.5+0.3	5.667	0.126	20.7
G6.1+0.5	6.055	0.499	6.1
G6.1+1.2	6.183	1.107	8.0
G6.4−0.1	6.485	−0.102	19.0
G6.5−0.4	6.521	−0.483	10.6
G7.0−0.1	7.075	−0.102	9.1
G7.2+0.2	7.204	0.177	4.9
G8.9+0.4	8.778	0.477	18.9
G8.7−0.1	8.828	−0.153	18.9
G9.7−0.0	9.682	−0.077	5.0
G9.8+0.6	9.781	0.571	7.5
G9.9−0.8	9.974	−0.822	6.2
G11.0−0.0	11.037	−0.053	4.5
G11.1−0.7	11.130	−0.775	8.4
G11.2−0.3	11.180	−0.348	2.8
G11.1+0.1	11.186	0.128	5.1
G11.4−0.1	11.383	−0.073	4.8
G12.0−0.1	11.964	−0.097	3.4
G12.2+0.3	12.262	0.305	3.4
G12.5+0.2	12.580	0.217	2.7
G12.7−0.0	12.712	−0.008	3.2
G12.8−0.0	12.819	−0.023	1.5
G13.1−0.5	13.078	−0.584	12.8
G13.5+0.2	13.454	0.139	2.6
G22.1−0.1	14.209	−0.076	11.3

Table 2, continued.

Name ^a	GLong ^b deg.	GLat deg.	Radius arcmin.
G15.4+0.1	15.427	0.161	7.3
G15.5−0.1	15.506	−0.148	5.4
G15.9+0.2	15.888	0.198	3.2
G16.0−0.5	16.053	−0.479	11.7
G16.7+0.1	16.735	0.082	2.6
G17.0−0.0	17.016	−0.035	2.5
G17.4−0.1	17.476	−0.117	5.0
G18.1−0.1	18.150	−0.170	4.6
G18.6−0.2	18.620	−0.280	3.4
G18.8+0.3	18.770	0.390	10.3
G18.9−1.1	18.950	−1.077	19.0
G19.1+0.2	19.240	0.260	20.2
G20.0−0.2	19.990	−0.190	7.3
G21.0−0.4	21.030	−0.470	5.6
G21.5−0.9	21.500	−0.885	1.5
G21.6−0.8	21.640	−0.830	8.1
G21.8−0.6	21.830	−0.520	15.5
G22.7−0.2	22.710	−0.200	13.9
G23.3−0.3	23.270	−0.330	16.8
G24.7+0.6	24.550	0.630	15.2
G24.7−0.6	24.860	−0.660	13.1
G27.4+0.0	27.390	−0.010	3.1
G27.8+0.6	27.700	0.630	23.4
G28.3+0.2	28.365	0.209	6.5
G28.6−0.1	28.610	−0.110	5.3
G28.7−0.4	28.784	−0.437	6.0
G29.6+0.1	29.564	0.110	3.1
G29.7−0.3	29.710	−0.237	2.4
G30.7+1.0	30.700	1.010	11.7
G31.5−0.6	31.544	−0.660	10.7
G31.9+0.0	31.870	0.017	4.1
G32.1−0.9	32.130	−0.960	21.5
G32.4+0.1	32.420	0.110	4.4
G32.8−0.1	32.790	−0.040	11.5
G33.2−0.6	33.180	−0.570	9.2
G33.6+0.1	33.670	0.030	6.7
G34.7−0.4	34.660	−0.400	19.2
G35.6−0.4	35.590	−0.440	8.6
G36.6−0.7	36.591	−0.818	6.5
G38.7−1.3	38.756	−1.151	25.1
G39.2−0.3	39.220	−0.320	4.5
G40.5−0.5	40.520	−0.510	12.5
G41.1−0.3	41.120	−0.314	2.7
G41.5+0.4	41.450	0.410	8.5
G42.0−0.1	41.960	−0.050	5.9
G42.8+0.6	42.773	0.666	13.4
G43.3−0.2	43.273	−0.182	3.1
G45.7−0.4	45.610	−0.390	14.0
G46.8−0.3	46.767	−0.280	10.0

Table 2, continued.

Name ^a	GLong ^b deg.	GLat deg.	Radius arcmin.
G49.2−0.7	49.185	−0.520	19.2
G53.4+0.0	53.416	0.042	4.2
G54.1+0.3	54.099	0.261	7.1
G54.4−0.3	54.500	−0.270	25.0
G55.0+0.3	54.935	−0.086	37.9
G57.2+0.8	57.240	0.820	6.7
G59.5+0.1	59.590	0.110	9.0

Notes. ^(a) The source names listed in G22. ^(b) Source centers and radii were determined by-eye from SMGPS data.

Table 3: Previously-Identified Objects From SNRCat

Name ^a	GLong deg.	GLat deg.	Radius arcmin.
G267.0−1.0	266.967	−1.005	0.5
G269.7+0.0	269.638	0.030	21.5
G284.0−1.8	284.079	−1.880	0.4
G291.0+0.1	291.011	0.079	13.3
G296.6−0.4	296.608	−0.388	6.8
G299.3−1.5	299.294	−1.521	18.5
G310.9−0.3	310.887	−0.262	8.4
G313.3+0.1	313.295	0.124	2.3
G313.6+0.3	313.594	0.318	7.4
G319.9−0.7	319.901	−0.674	5.1
G322.7+0.1	322.684	0.078	7.3
G322.9−0.0	322.886	−0.002	7.0
G324.1+0.0	324.117	0.046	5.1
G325.0−0.3	324.984	−0.315	2.1
G330.7+0.1	330.718	0.116	7.4
G333.9+0.0	333.863	−0.046	6.0
G334.0−0.8	333.895	−0.850	10.1
G336.4+0.2	336.386	0.191	0.5
G336.7−0.3	336.658	−0.300	2.7
G336.9−0.5	336.846	−0.550	8.5
G337.5−0.1	337.528	−0.111	3.9
G346.2−1.0	346.190	−0.984	4.0
G348.9−0.4	348.960	−0.455	20.5
G350.2−0.8	350.219	−0.842	0.6
G354.1+0.3	354.055	0.281	6.4
G5.7−0.1	5.699	−0.088	7.1
G18.0−0.7	18.001	−0.691	0.3
G20.4+0.1	20.460	0.150	5.4
G29.4+0.1	29.369	0.101	5.3
G36.0+0.1	36.008	0.057	0.2

Notes. ^(a) The source names listed in SNRCat. ^(b) Source centers and radii were determined by-eye from SMGPS data.

4.2. Previously-Identified SNR Candidates

We examine the SMGPS images for radio continuum emission from the 170 previously-known SNR candidates in the SMGPS zone. We find unambiguous SMGPS emission consistent with that of known SNRs from 130 SNR candidates. We list these detected SNR candidates in Table 4. In this table, as with the known SNRs, we revise the coordinates and sizes of the SNR candidates to enclose the SMGPS emission, but use the published source names. These names

are based on the published coordinates and have different numbers of significant digits between different authors.

We suggest that 13 previously-identified SNR candidates are misidentified. Although detected in SMGPS data, a different classification for these sources is warranted. Two are part of known SNRs (G6.4500–0.5583 is part of SNR G6.5–0.4 and G8.8583–0.2583 is part of G8.7–0.1). Three are confused with other SNR candidates (G005.989+0.019 with G006.199+0.157, G28.92+0.26 with G028.929+0.254, and G039.203+0.811 with G039.038+0.748). Five are confused with HII regions (G331.8–0.0 with G331.834–00.00, G002.228+0.058 with G2.227+0.058, G022.951–0.311 with G22.951–0.311, G028.524+0.268 with G028.647+00.198, and G037.506+0.777 with G037.506+0.777). Sources G324.4–0.2 and G327.1+0.9 (Ball et al. 2023) are MIPS-GAL bubbles, which are likely caused by an evolved star. Finally, G339.6–0.6 appears to be a radio galaxy.

Radiation will create ionized gas when impinging on a molecular cloud. Like in an HII region, this ionized gas will emit radio continuum emission and the associated heated dust grains will emit in the MIR. A low-density pathway through the interstellar medium would allow photons from a high-mass star formation region to irradiate clouds far afield, making this scenario possible whenever the ionizing flux in a region of the interstellar medium is high. The observational signature of this scenario is MIR emission spatially coincident with radio continuum emission, similar to that of an HII region, but the morphology will not have the generally circular symmetry of an HII region. For six previously-identified SNR candidates, we suggest that the emission is actually thermal, caused by irradiation from nearby star formation regions (G26.13+0.13, G028.877+0.241, G28.88+0.41, G34.93–0.24, G39.56–0.32, and G043.070+0.558).

Fifteen previously-identified SNR candidates appear to consist of nonthermal radio continuum emission (with no MIR), but the radio emission from each one does not form a cohesive structure (G005.106+0.332, G013.549+0.352, G013.626+0.299, G013.658–0.241, G016.126+0.690, G18.53–0.86, G19.13+0.90, G021.492–0.010, G022.177+0.314, G024.193+0.284, G27.39+0.24, G28.21+0.02, G030.362+0.623, G34.93–0.24, and G037.337+0.422). Most of these consist of a single broad radio filament. We suggest that these sources are poor SNR candidates that deserve future study.

While some previously-known SNR candidates are detected in the SMGPS, we decompose their emission into a number of new SNR candidates or find a dramatically different centroid. We decompose the SNR candidate G328.6+0.0 (Ball et al. 2023) into two regions. We decompose SNR candidate G323.6–1.1 (Ball et al. 2023) into two new SNR candidates and the known SNR G323.7–1.0. Finally, we revise the position of G325.8+0.3 substantially. These SNR candidates are not included in Table 4.

Ten SNR candidates are not detected in SMGPS data: G350.7+0.6, G353.0+0.8, G358.3–0.7, G18.9–1.2, G21.8+0.2, G24.0–0.3, G030.508+0.574, G32.73+0.15, G035.129–0.343, and G35.3–0.0. We can make no judgement on the veracity of these classifications. Most (6 of the 10) sources have angular sizes $> 30'$, which makes their detection difficult in SMGPS data. Two (G32.73+0.15 and G35.3–0.0) are in regions of the SMGPS with high noise.

Table 4: Previously-Identified SNR Candidates

Name ^a	GLong ^b deg.	GLat deg.	Radius arcmin.	Ref.
G304.437–0.229	304.437	–0.229	7.2	14
G317.5+0.9	317.550	0.953	16.3	13
G320.6–0.9	320.636	–0.926	1.7	13
G323.2–1.0	323.223	–0.977	4.2	13, 14
G323.7+0.0	323.720	–0.019	2.0	14
G324.1–0.2	324.099	–0.183	5.6	14
G324.3+0.2	324.265	0.244	2.3	14
G324.4–0.4	324.375	–0.369	8.0	14
G324.7+0.0	324.660	–0.013	2.2	14
G324.8–0.1	324.790	–0.100	11.9	14
G325.0–0.5	324.945	–0.477	16.3	14
G325.0+0.2	324.959	0.174	2.5	14
G328.0+0.7	328.035	0.677	4.6	14
SCO J170029–421309	343.874	0.032	2.2	17
SCO J165948–420527	343.918	0.182	3.4	17
G346.5–0.1	346.514	–0.080	6.3	16
G349.1–0.3	349.104	–0.825	6.0	5
G351.0–0.6	351.033	–0.627	6.0	5
G351.4+0.4	351.409	0.484	4.4	5
G351.4+0.2	351.470	0.205	7.6	5
G351.9+0.1	351.918	0.148	8.3	5
G001.949–0.100	1.949	–0.100	8.3	12
G001.975–0.460	1.975	–0.460	4.9	12
G002.228+0.058	2.228	0.058	1.1	12
G002.276+0.399	2.276	0.399	6.3	12
G002.910–0.183	2.910	–0.183	12.9	12
G003.101–0.093	3.101	–0.093	2.5	12
G003.103+0.110	3.103	0.110	1.4	12
G4.20–0.30	4.176	–0.261	4.0	1
G004.493–0.391	4.493	–0.391	6.9	12
G004.571–0.244	4.571	–0.244	4.2	12
G005.161–0.321	5.161	–0.321	5.6	12
G005.364–0.705	5.364	–0.705	10.0	12
G005.378–0.280	5.378	–0.280	2.2	12
G005.378+0.347	5.378	0.347	6.2	12
G005.762+0.515	5.762	0.515	5.8	12
G006.118+0.387	6.118	0.387	9.7	12
G6.31+0.54	6.247	0.458	10.5	2
G7.4+0.3	7.427	0.331	6.8	5
G008.040+0.566	8.050	0.566	5.0	12
G11.5500+0.3333	11.550	0.339	3.4	3
G013.500+0.074	13.500	0.074	1.9	12

Table 4, continued.

Name ^a	GLong deg.	GLat deg.	Radius arcmin.	Ref.
G013.652+0.259	13.652	0.259	2.5	12
G014.524+0.140	14.524	0.140	14.5	12
G015.862+0.522	15.862	0.522	1.9	12
G016.021+0.746	16.021	0.746	6.3	12
G016.956−0.933	16.956	−0.933	7.4	12
G017.434+0.273	17.434	0.273	2.1	12
G017.593+0.237	17.593	0.237	1.5	12
G017.620+0.086	17.620	0.086	3.0	12
G17.80−0.02	17.810	−0.018	4.3	4
G018.393−0.816	18.393	−0.816	2.6	12
G18.76−0.07	18.761	−0.074	1.2	2, 4
G019.481−0.108	19.481	−0.108	7.4	12
G19.75−0.69	19.746	−0.694	12.2	4, 5
G019.751+0.202	19.751	0.202	7.9	12
G19.96−0.33	19.960	−0.330	5.9	4
G020.195+0.028	20.195	0.028	3.6	12
G20.26−0.86	20.286	−0.858	8.6	4
G021.596−0.179	21.596	−0.179	10.4	12
G021.684+0.129	21.684	0.129	3.8	12
G021.861+0.169	21.861	0.169	2.7	12
G022.045−0.028	22.045	−0.028	7.7	12
G22.32+0.11	22.265	0.052	10.1	3, 4
G23.11+0.19	23.116	0.186	11.7	4, 5, 6
G23.85−0.18	23.855	−0.182	2.2	4
G023.973+0.510	23.973	0.510	4.9	12
G024.062−0.808	24.062	−0.808	2.0	12
G25.49+0.01	25.482	0.009	6.5	4, 7
G26.04−0.42	25.971	−0.392	11.4	4
G26.53+0.07	26.530	0.070	11.2	4
G26.75+0.73	26.753	0.693	7.2	4
G27.06+0.04	27.025	0.067	9.0	3, 4, 8
G27.18+0.30	27.179	0.303	1.3	4
G27.24−0.14	27.240	−0.140	6.1	4
G27.47+0.25	27.461	0.241	1.7	4
G27.78−0.33	27.776	−0.325	3.3	4
G28.22−0.09	28.216	−0.087	1.7	4
G28.33+0.06	28.330	0.060	3.2	4
G28.56+0.00	28.557	−0.012	2.3	3, 4, 8
G28.64+0.20	28.640	0.200	11.4	3, 4
G028.870+0.616	28.870	0.616	2.0	12
G028.929+0.254	28.929	0.254	2.2	12
G029.329+0.280	29.329	0.280	2.5	12
G29.41−0.18	29.410	−0.180	7.5	4
G030.303+0.128	30.303	0.128	1.0	12
G030.375+0.424	30.375	0.424	2.3	12
G31.22−0.02	31.256	−0.041	3.3	4
G31.93+0.16	31.937	0.171	2.3	4
G32.22−0.21	32.226	−0.210	3.2	4
G032.458−0.112	32.458	−0.112	1.8	12

Table 4, continued.

Name ^a	GLong deg.	GLat deg.	Radius arcmin.	Ref.
G33.85+0.06	33.847	0.062	0.5	4
G034.524−0.761	34.524	−0.761	2.7	12
G034.619+0.240	34.619	0.240	3.0	12
G36.66−0.50	36.660	−0.500	8.2	4
G36.68−0.14	36.671	−0.137	9.5	4
G036.839−0.433	36.839	−0.433	2.6	12
G036.851−0.246	36.851	−0.246	1.5	12
G36.90+0.49	36.902	0.488	3.8	4
G37.62−0.22	37.621	−0.219	2.2	4
G037.672−0.501	37.672	−0.501	2.8	12
G37.88+0.32	37.897	0.289	13.8	4
G38.17+0.09	38.138	0.056	10.5	4
G38.62−0.24	38.620	−0.240	2.5	4
G38.68−0.43	38.694	−0.453	2.6	4
G38.83−0.01	38.838	−0.012	1.3	4
G039.539+0.366	39.539	0.366	4.5	12
G041.510−0.534	41.510	−0.534	16.0	12
G041.625+0.261	41.625	0.241	4.7	12
G41.95−0.18	41.950	−0.180	7.0	4
G42.62+0.14	42.623	0.174	5.1	4
G042.711−0.272	42.711	−0.272	9.1	12
G043.023+0.726	43.011	0.746	6.5	12
G043.502+0.667	43.502	0.667	10.1	15
G044.076+0.127	44.076	0.127	8.0	12
G46.18−0.02	46.155	−0.020	6.5	4
G46.54−0.03	46.542	0.004	8.2	4
G47.15+0.73	47.150	0.730	0.8	4
G047.741−0.971	47.741	−0.971	9.8	12
G048.875+0.174	48.875	0.174	6.6	12
G051.061+0.563	51.061	0.563	4.7	12
G51.21+0.11	51.209	0.113	14.9	4, 8, 9, 10
G52.37−0.70	52.381	−0.725	18.9	4, 10
G53.07+0.49	53.071	0.490	0.9	4, 10
G53.84−0.75	53.840	−0.750	18.7	4, 10
G56.56−0.75	56.502	−0.774	13.1	4
G57.12+0.35	57.114	0.331	13.5	4
G58.70−0.31	58.697	−0.314	4.0	4
G59.46+0.83	59.455	0.819	3.8	4
G059.834−0.405	59.834	−0.405	10.5	12

Notes. ^(a) The source names in the original publications.
^(b) Source centers and radii were determined by-eye from SMGPS data.

References. (1) [Trushkin \(2001\)](#); (2) [Brogan et al. \(2006\)](#); (3) [Helfand et al. \(2006\)](#); (4) [Anderson et al. \(2017\)](#); (5) [Hurley-Walker et al. \(2019\)](#); (6) [Maxted et al. \(2019\)](#); (7) [Bamba et al. \(2003\)](#); (8) [Dokara et al. \(2018\)](#); (9) [Sidorin et al. \(2014\)](#); (10) [Driessen et al. \(2018\)](#); (11) [Supan et al. \(2018\)](#); (12) [Dokara et al. \(2021\)](#); (13) [Whiteoak & Green \(1996\)](#); (14) [Ball et al. \(2023\)](#); (15) [Sushch et al. \(2017\)](#); (16) [Kaplan et al. \(2002\)](#); (17) [Gaensler et al. \(2001\)](#);

4.3. Newly-Identified SNR Candidates

By visually inspecting SMGPS and MIR data, we identify 237 new SNR candidates. All 237 SNR candidates have SMGPS 1.3 GHz continuum emission and a deficiency of MIR emission.

For each candidate, we assign a reliability criterion that indicates our confidence that the object is a true SNR

ranging from “I” (high reliability) to “III” (low reliability)⁸. Sources with a reliability criterion of “I” have clear SMGPS emission that is not confused with that of other SNRs or HII regions, with a morphology that is similar to that of known SNRs. These are most likely to have a shell morphology. Sources with a reliability criterion of “II” are either somewhat confused with that of other SNRs or HII regions, or which have a morphology that is slightly ambiguous. They may be cospatial with MIR emission, but we cannot be sure if this emission comes from the radio source or another region along the line of sight. Class II sources may also be incomplete shells. Sources with a reliability criterion of “III” are either badly confused with other SNRs or HII regions, have spatially coincident radio and MIR emission that may indicate that at least some of the radio emission is thermal, or are incomplete shells. We assign 35% of the newly-discovered SNR candidates a reliability criterion of “I,” 44% of “II,” and 22% as “III.”

We give the parameters of the new SNR candidates in Table 5 and show two examples of each reliability criterion in Figure 5.

Table 5: SMGPS SNR Candidates

Name	GLong deg.	GLat deg.	Radius arcmin.	Reliability ^a
G257.408−00.162	257.408	−0.162	35.6	I
G259.683−01.235	259.683	−1.235	7.7	I
G275.256−00.979	275.256	−0.979	17.2	I
G275.986−01.077	275.986	−1.077	4.8	I
G276.229+00.419	276.229	0.419	1.5	II
G277.162+00.396	277.162	0.396	4.8	II
G278.924−01.195	278.924	−1.195	24.1	II
G280.151+00.206	280.151	0.206	12.8	I
G281.188−00.053	281.188	−0.053	29.1	I
G282.674−00.737	282.674	−0.737	10.4	I
G283.234−00.945	283.234	−0.945	6.4	II
G283.429−01.414	283.429	−1.414	10.4	II
G283.629−00.933	283.629	−0.933	10.2	II
G283.849−01.431	283.849	−1.431	9.9	III
G286.667+00.909	286.667	0.909	6.5	II
G286.825+00.025	286.825	0.025	21.2	II
G288.824−00.155	288.824	−0.155	2.7	II
G288.830−01.366	288.830	−1.366	20.0	III
G288.863−00.046	288.863	−0.046	20.6	III
G289.150−00.890	289.150	−0.890	15.6	I
G290.003−01.510	290.003	−1.510	4.3	II
G290.575+00.465	290.575	0.465	15.0	II
G292.313+00.587	292.313	0.587	9.5	II
G292.472+00.167	292.472	0.167	0.9	III
G295.855−01.388	295.855	−1.388	0.9	III
G297.038−01.010	297.038	−1.010	31.2	II
G299.680−00.015	299.680	−0.015	12.0	I
G302.324−01.300	302.324	−1.300	6.0	II
G303.365−00.050	303.365	−0.050	21.3	III

Table 5, continued.

Name	GLong deg.	GLat deg.	Radius arcmin.	Reliability ^a
G304.071+01.227	304.071	1.227	3.5	II
G304.226−00.504	304.226	−0.504	5.3	I
G306.195−00.520	306.195	−0.520	1.9	II
G306.243−00.876	306.243	−0.876	13.4	III
G307.050−00.691	307.050	−0.691	31.4	I
G307.510−00.954	307.510	−0.954	11.1	I
G307.930+00.134	307.930	0.134	13.8	I
G308.309−00.189	308.309	−0.189	5.9	II
G308.730+01.380	308.730	1.380	10.8	I
G308.830−00.544	308.830	−0.544	15.6	I
G309.202−00.118	309.202	−0.118	6.7	I
G310.275−00.171	310.275	−0.171	5.2	I
G310.457−00.607	310.457	−0.607	12.4	I
G310.702−00.573	310.702	−0.573	1.2	II
G310.955−00.565	310.955	−0.565	2.6	II
G312.273−00.673	312.273	−0.673	9.7	I
G312.504−00.018	312.504	−0.018	1.1	II
G312.969−00.095	312.969	−0.095	8.1	I
G313.499−00.525	313.499	−0.525	7.9	I
G314.338−00.204	314.338	−0.204	12.8	I
G314.620+00.256	314.620	0.256	12.0	III
G315.312−00.319	315.312	−0.319	7.1	I
G315.715−00.227	315.715	−0.227	0.9	II
G315.501−00.584	315.501	−0.584	1.6	II
G315.620+00.332	315.620	0.332	2.6	II
G315.905−00.817	315.905	−0.817	13.2	II
G316.349−00.340	316.349	−0.340	10.5	I
G316.456−00.095	316.456	−0.095	1.4	II
G316.587−00.097	316.587	−0.097	4.9	III
G316.704+00.399	316.704	0.399	7.3	I
G318.033−00.935	318.033	−0.935	1.5	II
G318.072−00.394	318.072	−0.394	4.0	II
G318.602−00.884	318.602	−0.884	9.2	II
G318.871−00.468	318.871	−0.468	9.0	I
G319.426−00.691	319.426	−0.691	9.4	I
G320.762−00.351	320.762	−0.351	5.0	I
G320.944−01.289	320.944	−1.289	7.4	III
G321.311−00.862	321.311	−0.862	3.5	I
G321.455+00.408	321.455	0.408	6.4	III
G322.462+00.084	322.462	0.084	9.7	III
G322.644−00.694	322.644	−0.694	15.0	I
G322.762−00.423	322.762	−0.423	9.5	I
G323.551−00.190	323.551	−0.190	27.2	I
G323.552−00.790	323.552	−0.790	15.6	I
G323.884−01.128	323.884	−1.128	14.6	I
G324.009−01.295	324.009	−1.295	1.2	III
G324.505+00.128	324.505	0.128	3.5	III
G324.923−00.571	324.923	−0.571	5.7	II
G325.502+00.293	325.502	0.293	29.1	II
G326.622−00.558	326.622	−0.558	28.8	III
G328.225−00.664	328.225	−0.664	5.5	I
G328.346−00.480	328.346	−0.480	2.8	II
G328.479−00.108	328.479	−0.108	9.3	I
G328.703+00.016	328.703	0.016	9.3	I

⁸ See Brogan et al. (2006) and Hurley-Walker et al. (2019), who used the same nomenclature with slightly different definitions.

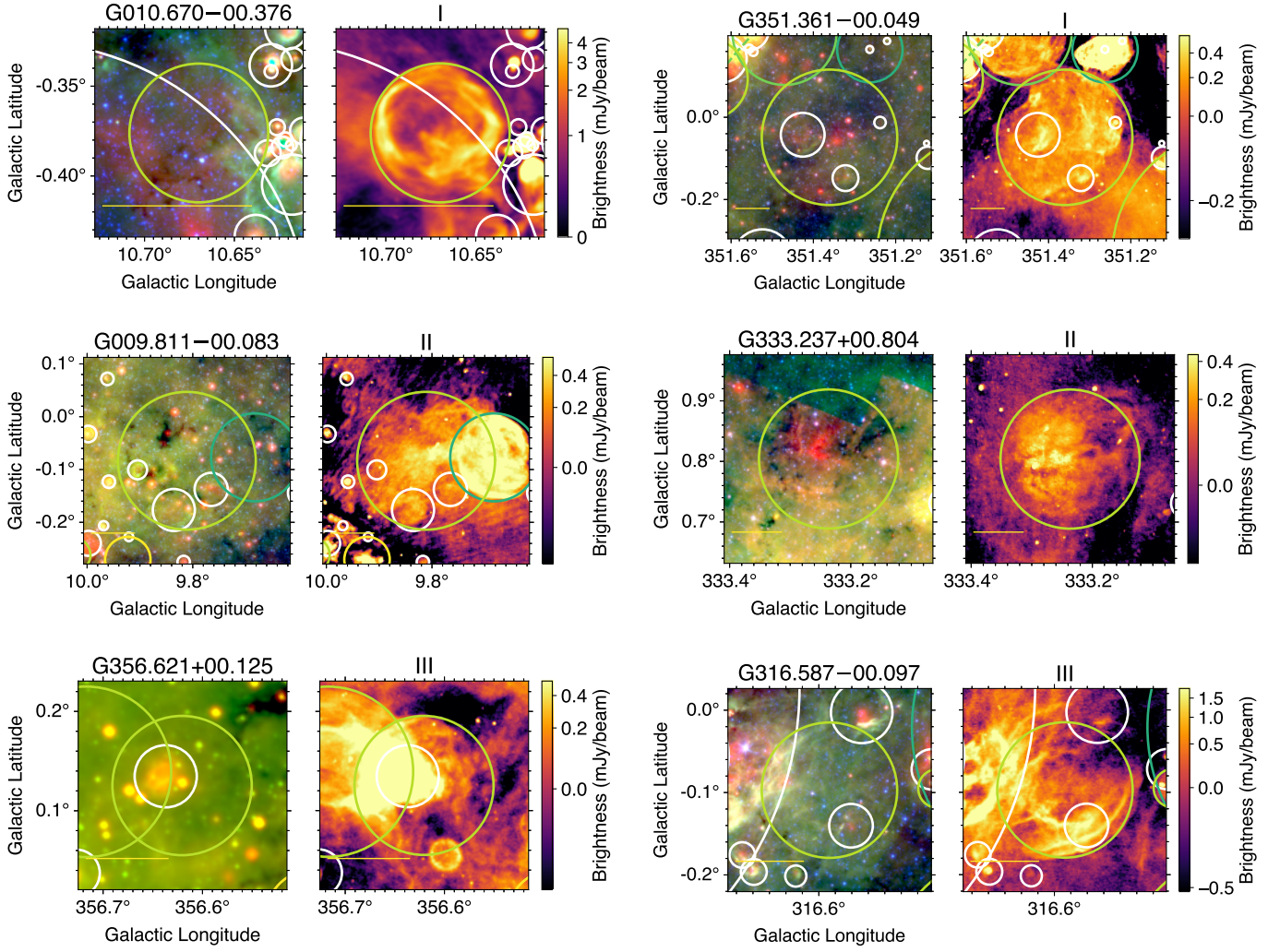


Fig. 5: Example newly-discovered SNR candidates. MIR data is in the left panels and SMGPS 1.3 GHz data are on the right. The symbols have the same meaning as in Figure 1, with the candidate SNRs being represented by light green circles at the centers of all panels. On the top of the panels showing SMGPS images we list our reliability classification, with “I” being the most reliable and “III” the least. Yellow scale bars at the lower left of each panel are 5' long.

Table 5, continued.

Name	GLong deg.	GLat deg.	Radius arcmin.	Reliability ^a
G330.628-00.284	330.628	-0.284	7.7	I
G331.635+00.247	331.635	0.247	14.7	I
G332.478+00.083	332.478	0.083	3.9	I
G333.237+00.804	333.237	0.804	6.9	II
G333.480+00.010	333.480	0.010	7.1	II
G334.038+00.040	334.038	0.040	5.9	I
G334.834-00.044	334.834	-0.044	0.9	II
G334.929-00.464	334.929	-0.464	4.2	I
G334.938-00.319	334.938	-0.319	1.8	II
G334.991-00.290	334.991	-0.290	1.0	III
G335.179+00.525	335.179	0.525	7.0	II
G335.341-00.189	335.341	-0.189	1.7	II
G335.386+00.252	335.386	0.252	5.9	II
G336.321-00.748	336.321	-0.748	1.0	II
G337.031-00.210	337.031	-0.210	2.5	III

Table 5, continued.

Name	GLong deg.	GLat deg.	Radius arcmin.	Reliability ^a
G337.069-00.340	337.069	-0.340	1.3	III
G337.109-00.066	337.109	-0.066	1.3	II
G337.167+00.332	337.167	0.332	2.5	II
G338.763+00.374	338.763	0.374	11.5	III
G339.169-00.023	339.169	-0.023	1.2	III
G339.190-00.266	339.190	-0.266	6.5	I
G339.304+00.038	339.304	0.038	5.6	III
G339.446-00.151	339.446	-0.151	1.1	I
G339.686-00.182	339.686	-0.182	4.2	I
G340.132-00.069	340.132	-0.069	3.1	II
G340.763-00.463	340.763	-0.463	7.4	II
G341.137-01.237	341.137	-1.237	2.1	II
G341.427-00.393	341.427	-0.393	4.2	II
G341.456-00.176	341.456	-0.176	7.8	I
G341.515+00.174	341.515	0.174	13.7	II

Table 5, continued.

Name	GLong deg.	GLat deg.	Radius arcmin.	Reliability ^a
G341.756−00.324	341.756	−0.324	5.8	I
G341.830−00.591	341.830	−0.591	14.0	III
G341.997−00.007	341.997	−0.007	13.7	III
G342.065+01.000	342.065	1.000	33.2	II
G342.427+00.472	342.427	0.472	18.8	II
G342.556+00.615	342.556	0.615	7.5	I
G342.731+00.172	342.731	0.172	2.7	II
G343.326−00.335	343.326	−0.335	5.0	II
G343.591−00.071	343.591	−0.071	12.6	II
G344.064−00.013	344.064	−0.013	6.6	III
G345.167−00.172	345.167	−0.172	6.4	II
G345.308−01.077	345.308	−1.077	3.4	II
G345.532−00.001	345.532	−0.001	4.4	I
G345.821+01.199	345.821	1.199	10.5	II
G345.899+00.169	345.899	0.169	4.3	I
G346.072+00.040	346.072	0.040	2.3	II
G346.365+00.305	346.365	0.305	3.8	III
G346.821−00.981	346.821	−0.981	6.0	III
G346.849+00.353	346.849	0.353	3.5	II
G346.907+00.323	346.907	0.323	1.0	II
G347.362−00.352	347.362	−0.352	15.8	I
G347.380+00.473	347.380	0.473	19.0	II
G348.160−00.211	348.160	−0.211	12.0	II
G348.324−00.735	348.324	−0.735	4.7	I
G348.374+00.153	348.374	0.153	9.0	I
G348.586+00.249	348.586	0.249	7.3	I
G350.299−00.086	350.299	−0.086	9.7	I
G350.404−01.013	350.404	−1.013	2.6	II
G350.471+00.088	350.471	0.088	1.3	II
G350.584−00.909	350.584	−0.909	2.8	II
G350.937−00.338	350.937	−0.338	18.5	II
G351.361−00.049	351.361	−0.049	9.9	I
G351.658+00.093	351.658	0.093	5.9	I
G351.790−00.239	351.790	−0.239	7.7	II
G352.220−00.458	352.220	−0.458	18.1	II
G352.267−00.062	352.267	−0.062	7.4	I
G352.589−00.299	352.589	−0.299	7.4	II
G352.759−00.340	352.759	−0.340	5.4	I
G354.353−00.018	354.353	−0.018	2.3	II
G354.353−00.018	354.353	−0.018	2.3	II
G354.362+00.285	354.362	0.285	9.9	II
G354.931−00.241	354.931	−0.241	2.9	II
G355.406+00.513	355.406	0.513	3.5	II
G355.464−00.253	355.464	−0.253	3.0	II
G355.854−00.084	355.854	−0.084	1.0	III
G355.919−00.206	355.919	−0.206	2.0	I
G356.621+00.125	356.621	0.125	4.2	III
G356.662−00.297	356.662	−0.297	12.8	II
G356.717+00.139	356.717	0.139	5.1	II
G356.795−00.073	356.795	−0.073	0.8	II
G357.083+00.318	357.083	0.318	3.2	I
G357.109−00.187	357.109	−0.187	9.0	I
G357.109+00.055	357.109	0.055	5.2	I
G357.528−00.455	357.528	−0.455	11.2	III

Table 5, continued.

Name	GLong deg.	GLat deg.	Radius arcmin.	Reliability ^a
G357.976−00.145	357.976	−0.145	0.9	II
G358.280−00.850	358.280	−0.850	14.0	I
G358.282+00.069	358.282	0.069	2.5	II
G358.398+00.090	358.398	0.090	2.6	I
G001.964−00.573	1.964	−0.573	1.2	III
G002.684+00.032	2.684	0.032	12.2	III
G003.270+00.128	3.270	0.128	5.6	II
G003.656−00.124	3.656	−0.124	5.5	III
G004.215+00.351	4.215	0.351	0.7	II
G005.522+01.080	5.522	1.080	7.6	II
G005.996−00.577	5.996	−0.577	1.3	II
G006.234−00.784	6.234	−0.784	1.2	III
G006.249−00.757	6.249	−0.757	0.9	III
G006.609−00.608	6.609	−0.608	11.7	II
G007.374−00.149	7.374	−0.149	6.0	III
G007.377+00.716	7.377	0.716	12.3	I
G008.240+00.472	8.240	0.472	18.4	III
G008.482+00.202	8.482	0.202	11.4	III
G009.211+00.063	9.211	0.063	4.7	II
G009.367+00.444	9.367	0.444	12.9	II
G009.811−00.083	9.811	−0.083	7.8	II
G010.026−00.262	10.026	−0.262	1.9	II
G010.670−00.376	10.670	−0.376	2.3	I
G012.014−00.576	12.014	−0.576	6.4	I
G012.864+00.010	12.864	0.010	9.8	III
G013.155−00.797	13.155	−0.797	4.8	II
G013.313−00.695	13.313	−0.695	6.6	III
G013.593−00.377	13.593	−0.377	6.8	II
G014.223−00.174	14.223	−0.174	13.2	III
G017.218−00.077	17.218	−0.077	4.9	II
G021.466+00.135	21.466	0.135	6.2	III
G023.293−00.563	23.293	−0.563	10.2	II
G026.902+00.240	26.902	0.240	5.1	III
G032.582+00.779	32.582	0.779	2.3	II
G035.997+00.957	35.997	0.957	11.2	III
G036.245+00.350	36.245	0.350	10.5	II
G036.858+00.083	36.858	0.083	5.6	II
G037.455−00.282	37.455	−0.282	4.7	III
G037.518−00.631	37.518	−0.631	3.5	II
G037.693+01.814	37.693	1.814	58.0	III
G037.877+00.593	37.877	0.593	3.1	II
G038.214−00.202	38.214	−0.202	1.0	II
G038.815−00.136	38.815	−0.136	4.3	I
G039.038+00.748	39.038	0.748	11.7	I
G039.516+00.501	39.516	0.501	6.1	I
G040.341+00.277	40.341	0.277	1.6	II
G040.449+00.540	40.449	0.540	9.1	I
G040.866+00.155	40.866	0.155	10.6	II
G041.699+00.975	41.699	0.975	3.0	II
G042.186−00.802	42.186	−0.802	2.0	II
G042.506−00.445	42.506	−0.445	1.7	III
G042.665−00.634	42.665	−0.634	1.8	III
G042.954+00.074	42.954	0.074	4.4	I
G043.047−00.067	43.047	−0.067	5.4	I

Table 5, continued.

Name	GLong deg.	GLat deg.	Radius arcmin.	Reliability ^a
G046.304+00.352	46.304	0.352	11.2	III
G046.577+00.221	46.577	0.221	9.0	III
G043.942+01.442	43.942	1.442	8.1	I
G044.106+00.595	44.106	0.595	24.2	III
G044.339+01.273	44.339	1.273	2.5	I
G046.420+00.169	46.420	-0.169	9.3	I
G046.910+00.114	46.910	0.114	7.3	I
G050.489+00.410	50.489	-0.410	8.9	II
G051.746+01.384	51.746	1.384	8.6	II
G055.226+00.477	55.226	0.477	16.4	III
G056.116+00.294	56.116	0.294	2.9	II
G057.423+00.864	57.423	0.864	11.9	I
G057.675+00.676	57.675	0.676	11.9	I
G057.868+00.221	57.868	0.221	8.4	I
G057.884+00.543	57.884	0.543	11.9	I
G058.285+00.307	58.285	0.307	1.7	II

Notes. ^(a) “I” is most reliable and have clear SMGPS emission that is not confused with that of other SNRs or H II regions, with a morphology that is similar to that of known SNRs; “II” is less reliable and are either in confused regions with other SNRs or H II regions or have a morphology that is slightly ambiguous; “III” are the least reliable and are either badly confused with other SNRs or H II regions, have spatially coincident radio and MIR emission that may indicate that at least some of the radio emission is thermal, or are incomplete shells.

4.4. Unusual Sources

We identify 49 unusual sources of radio continuum emission. These sources do not have the expected radio morphology for SNRs (or H II regions) but they do lack MIR emission. Included in this list is known SNR G298.5–00.3 (Figure 4). These objects may be SNRs, but because they lack the characteristic SNR radio morphologies, we do not include them in the SNR candidates list. They are worthy of future study. We list the position and circular size of these regions in Table 6 and show examples in Figure 6.

Table 6: Unusual SMGPS Sources

Name	GLong deg.	GLat deg.	Radius arcmin.
G274.523–01.021	274.523	-1.021	5.6
G279.423–01.431	279.423	-1.431	4.2
G282.022–00.782	282.022	-0.782	2.2
G284.217+00.400	284.217	0.400	8.6
G289.104–00.563	289.104	-0.563	2.9
G293.650–00.229	293.650	-0.229	8.5
G298.516–00.352	298.516	-0.352	4.2
G301.980–00.316	301.980	-0.316	1.2
G310.863+00.011	310.863	0.011	1.1
G314.085–00.486	314.085	-0.486	6.0
G315.487–00.790	315.487	-0.790	0.6
G319.685+00.121	319.685	0.121	2.1
G322.113+00.879	322.113	0.879	6.7

Table 6, continued.

Name	GLong deg.	GLat deg.	Radius arcmin.
G324.067–00.581	324.067	-0.581	4.3
G324.633–00.410	324.633	-0.410	1.8
G325.709+00.959	325.709	0.959	10.5
G329.877–00.458	329.877	-0.458	0.7
G332.176+01.426	332.176	1.426	1.0
G332.228+00.198	332.228	0.198	1.1
G336.953–00.046	336.953	-0.046	2.1
G337.412+00.077	337.412	0.077	2.9
G339.388+00.700	339.388	0.700	1.7
G341.503–00.424	341.503	-0.424	0.9
G344.833–00.028	344.833	-0.028	1.6
G345.685+00.193	345.685	0.193	1.0
G345.884–00.172	345.884	-0.172	2.1
G346.169–00.419	346.169	-0.419	5.0
G346.366+00.105	346.366	0.105	3.1
G346.378–00.024	346.378	-0.024	2.1
G351.058+00.022	351.058	0.022	2.2
G354.136–00.185	354.136	-0.185	2.4
G354.191+00.620	354.191	0.620	7.9
G354.299–00.066	354.299	-0.066	1.3
G355.946+00.192	355.946	0.192	3.3
G356.489–00.007	356.489	-0.007	2.8
G001.708–00.145	1.708	-0.145	3.3
G001.763+00.057	1.763	0.057	2.4
G002.361–00.134	2.361	-0.134	9.5
G002.805+00.131	2.805	0.131	3.1
G005.489–00.350	5.489	-0.350	5.5
G006.195+00.651	6.195	0.651	2.7
G009.923–00.270	9.923	-0.270	2.6
G013.379+00.138	13.379	0.138	5.4
G017.307+00.095	17.307	0.095	2.7
G018.513+00.077	18.513	0.077	7.9
G019.175+00.653	19.175	0.653	3.7
G019.225+00.823	19.225	0.823	3.0
G043.335–00.252	43.335	-0.252	1.1
G051.564+00.095	51.564	0.095	0.7

4.5. Comparison Between the Galactic SNR, SNR Candidate, and H II Region Populations

The areal distributions of SNRs and SNR candidates, shown in Figure 7, are visually similar to each other. To assess whether the various samples are statistically distinct, we use a Kolmogorov-Smirnov (K-S) test, adopting $p = 0.001$ as the discriminating value such that statistically distinct samples will have $p < 0.001$.

We show the Galactic longitude distributions in the left panel of Figure 8. Because of the increased sensitivity of the SMGPS data compared to that previously available, there are far more newly-identified SNR candidates in the fourth versus the first Galactic quadrant (72 versus 28%). SNRs are more prevalent relative to H II regions between $300^\circ < \ell < 250^\circ$. The SNR candidate longitude distribution (including all SMGPS SNR candidates and those previously identified) is not statistically distinct from the known SNR distribution ($p = 0.017$).

We show the Galactic latitude distributions in the right panel of Figure 8. The SNR candidate latitude distribution (including all SMGPS SNR candidates and those previously identified) is not statistically distinct from the known SNR distribution ($p = 0.26$). Least-squares fits to the binned Galactic latitude distributions of known and candidate SNRs (including both previously-known and SMGPS discovered) have full width at half maximum (FWHM) val-

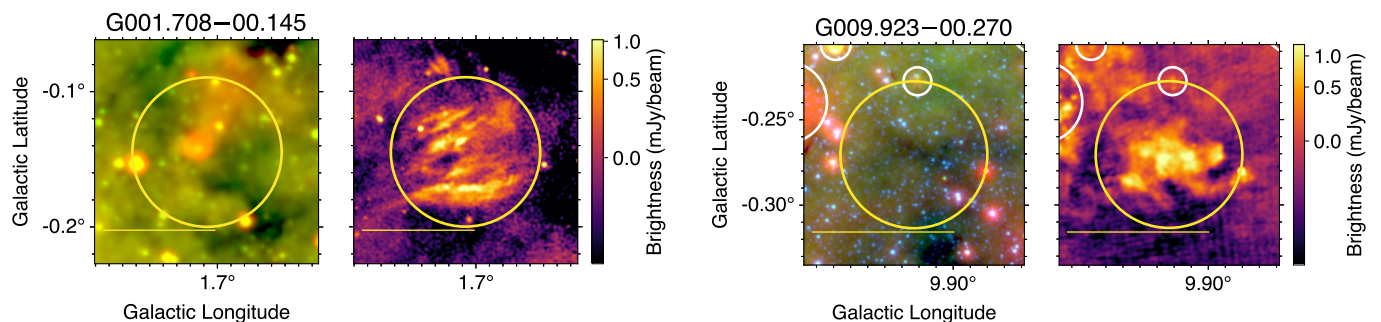


Fig. 6: Example unusual sources of SMGPS emission. MIR data is in the left panels (Spitzer or WISE) and SMGPS 1.3 GHz data are on the right. The symbols have the same meaning as in Figure 1, with the unusual sources being represented by yellow circles at the centers of all panels. Yellow scale bars at the lower left of each panel are 5' long.

ues of 0.97° , and 1.08° , respectively. The H II region distribution has a higher percentage of sources near $b = 0^\circ$; its FWHM fit value is 0.75° . Measured from the standard deviation σ , however, all three samples have similar FWHM values (FWHM = 2.354σ). We find the FWHM for the samples of known SNRs, candidate SNRs, and H II regions is 1.29° , 1.25° , and 1.22° , respectively.

As shown in Fig. 9, the known and candidate SNR angular radius distributions are similar, but the SNR candidate distributions have a higher percentage of sources at lower values. A K-S test indicates that they are marginally statistically distinct ($p = 0.001$). Given the higher angular resolution of recent radio surveys whose data has been used to identify SNR candidates (e.g., THOR, GLOSTAR, and the SMGPS), this difference is unsurprising.

4.6. Implications for the Galactic SNR population

If confirmed (i.e. with radio spectral index or polarization measurements, or with optical or x-ray searches), the 237 new SNR candidates would approximately double the known SNR population in the survey zone and would increase the total Galactic SNR population by $\sim 80\%$ (using the G22 number). Even if all SNR candidates are confirmed, however, there would probably be hundreds to thousands of Galactic SNRs that are yet to be identified (see Section 1). Future radio continuum surveys will hopefully find them.

5. Summary

Using 1.3 GHz continuum data from the MeerKAT Galactic Plane survey we cataloged 237 new Galactic SNR candidates. Our method identifies diffuse radio continuum emission regions lacking the MIR emission counterparts that would be seen for H II regions and planetary nebulae. All candidates lack MIR emission from known H II regions, as cataloged in the WISE Catalog of Galactic H II Regions. The detected candidates follow a similar areal distribution and have similar radii compared to the previously-identified sample.

We also detect radio continuum emission and confirm the expected morphology for 201 known SNRs: 184 from Green (2022) and 30 from Ferrand & Safi-Harb (2012). We identify two SNRs from Green (2022) and 21 from Ferrand & Safi-Harb (2012) that we believe should be reclassified.

If our candidates prove to be true SNRs, they would approximately double the Galactic SNR population in the surveyed region and increase the known SNR population by $\sim 80\%$. Although this is still fewer than expected for a Milky Way-type galaxy, the discrepancy is far less severe than it was a few years ago. There are now > 300 Galactic SNR candidates, indicating the need for followup observations.

Acknowledgements. We thank the anonymous referee for constructive comments that increased the clarity and readability of this work. The MeerKAT telescope is operated by the South African Radio Astronomy Observatory, which is a facility of the National Research Foundation, an agency of the Department of Science and Innovation. This research has made use of the SIMBAD database, operated at CDS, Strasbourg, France. LDA thanks Cara Gillotti for her invaluable help drawing green circles. LDA and TF acknowledge support from NSF ASTR #2307176. The National Radio Astronomy Observatory is a facility of the National Science Foundation operated under cooperative agreement by Associated Universities, Inc.

References

- Anderson, L. D., Bania, T. M., Balser, D. S., et al. 2014, *ApJS*, 212, 1
- Anderson, L. D., Bania, T. M., Balser, D. S., & Rood, R. T. 2011, *ApJS*, 194, 32
- Anderson, L. D., Wang, Y., Bihr, S., et al. 2017, *A&A*, 605, A58
- Armentrout, W. P., Anderson, L. D., Wenger, T. V., Balser, D. S., & Bania, T. M. 2021, *ApJS*, 253, 23
- Ball, B. D., Kothes, R., Rosolowsky, E., et al. 2023, *MNRAS*, 524, 1396
- Bamba, A., Ueno, M., Koyama, K., & Yamauchi, S. 2003, *ApJ*, 589, 253
- Benjamin, R. A., Churchwell, E., Babler, B. L., et al. 2003, *PASP*, 115, 953
- Beuther, H., Bihr, S., Rugel, M., et al. 2016, *A&A*, 595, A32
- Bietenholz, M. F. & Bartel, N. 2008, *MNRAS*, 386, 1411
- Bietenholz, M. F., Yuan, Y., Buehler, R., Lobanov, A. P., & Blandford, R. 2015, *MNRAS*, 446, 205
- Brogan, C. L., Gelfand, J. D., Gaensler, B. M., Kassim, N. E., & Lazio, T. J. W. 2006, *ApJ*, 639, L25
- Camilo, F., Scholz, P., Serylak, M., & et al. 2018, *ApJ*, 856, 180
- Carey, S. J., Noriega-Crespo, A., Mizuno, D. R., et al. 2009, *PASP*, 121, 76
- Churchwell, E., Babler, B. L., Meade, M. R., et al. 2009, *PASP*, 121, 213

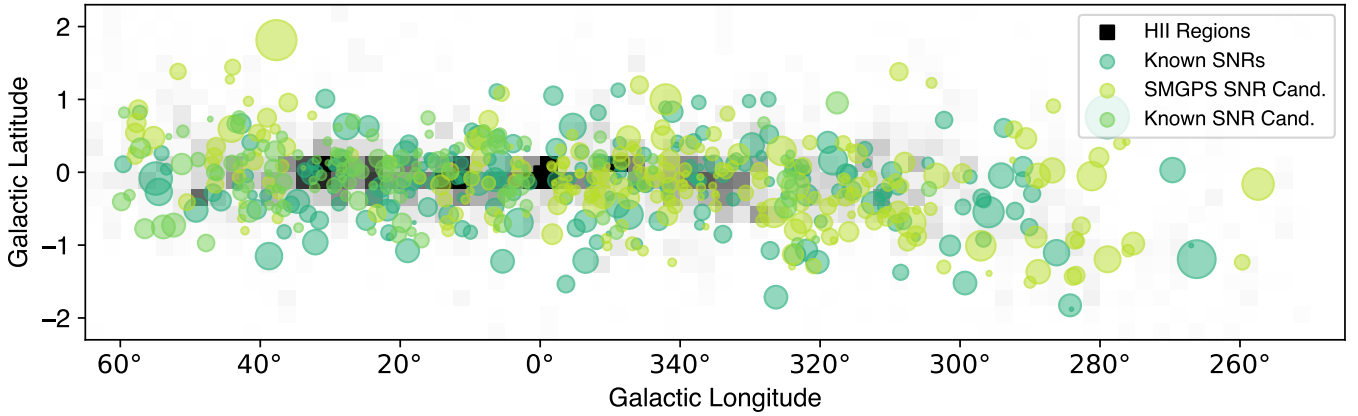


Fig. 7: Galactic distribution of the previously-known SNRs (blue-green, from both the G22 and SNRCat samples), SMGPS SNR candidates (light green filled), and previously-known SNR candidates (green open). The circles are representative of the SNR sizes. Only sources confirmed here are shown. The background is a two-dimensional histogram of the H II region density from the WISE Catalog, with higher densities indicated by darker shades.

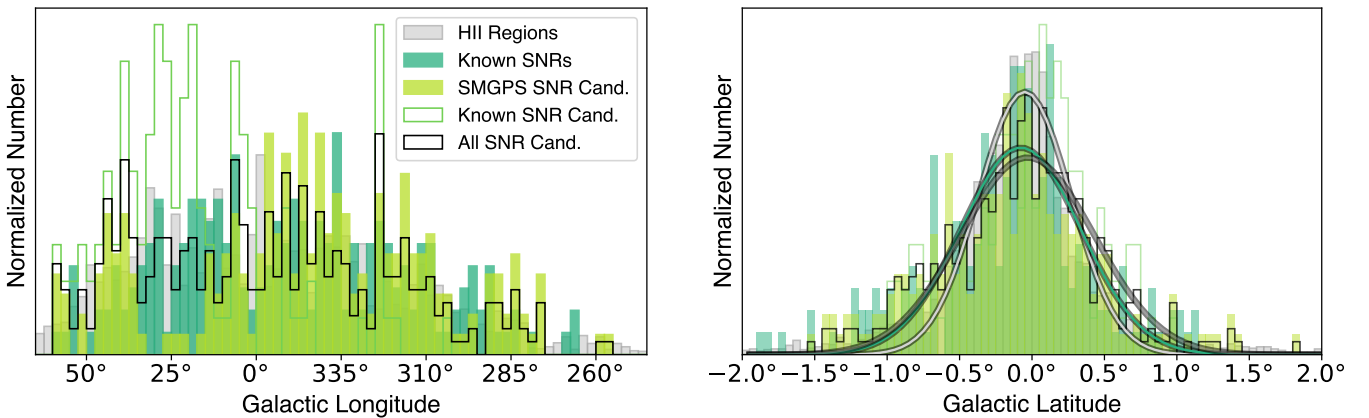


Fig. 8: Galactic longitude (left) and latitude (right) distributions for WISE Catalog H II regions (grey), known SNRs (blue-green, from both the G22 and SNRCat samples), SMGPS SNR candidates (light green filled), previously-known SNR candidates (green open), and all SNR candidates (SMGPS-discovered and previously-known combined; black open). Only sources confirmed here are shown. Curves in the right panel show least-squares fits to the binned distributions - the grey curve for H II regions, the blue-green curve for known SNRs, and the black curve for all SNR candidates.

- Cohen, M. & Green, A. J. 2001, *MNRAS*, 325, 531
- Cotton, W. D., Kothes, R., Camilo, F., et al. 2024, *ApJS*, 270, 21
- de Avillez, M. A. & Breitschwerdt, D. 2005, *A&A*, 436, 585
- Dokara, R., Brunthaler, A., Menten, K. M., et al. 2021, arXiv e-prints, arXiv:2103.06267
- Dokara, R., Roy, N., Beuther, H., et al. 2018, *ApJ*, 866, 61
- Driessen, L. N., Domček, V., Vink, J., et al. 2018, *ApJ*, 860, 133
- Dubner, G. & Giacani, E. 2015, *A&A Rev.*, 23, 3
- Faucher-Giguère, C.-A., Quataert, E., & Hopkins, P. F. 2013, *MNRAS*, 433, 1970
- Ferrand, G. & Safi-Harb, S. 2012, *Advances in Space Research*, 49, 1313
- Gaensler, B. M., Slane, P. O., Gotthelf, E. V., & Vasisht, G. 2001, *ApJ*, 559, 963
- Girichidis, P., Walch, S., Naab, T., et al. 2016, *MNRAS*, 456, 3432
- Goedhart, S., Cotton, W. D., Camilo, F., et al. 2024, *MNRAS*, 531, 649
- Gonçalves, D. P., Noriega-Crespo, A., Paladini, R., Martin, P. G., & Carey, S. J. 2011, *The Astronomical Journal*, 142, 47
- Green, A. J., Reeves, S. N., & Murphy, T. 2014, *PASA*, 31, e042
- Green, D. A. 2004, *Bulletin of the Astronomical Society of India*, 32, 335
- Green, D. A. 2014, *Bulletin of the Astronomical Society of India*, 42, 47
- Green, D. A. 2015, *MNRAS*, 454, 1517
- Green, D. A. 2022, *A Catalogue Galactic Supernova Remnants (2022 December version)*
- Helfand, D. J., Becker, R. H., White, R. L., Fallon, A., & Tuttle, S. 2006, *AJ*, 131, 2525
- Hurley-Walker, N., Gaensler, B. M., Leahy, D. A., et al. 2019, *PASA*, 36, e048
- Jonas, J. & MeerKAT Team. 2016, in *MeerKAT Science: On the Pathway to the SKA*, 1
- Joung, M. R., Mac Low, M.-M., & Bryan, G. L. 2009, *ApJ*, 704, 137

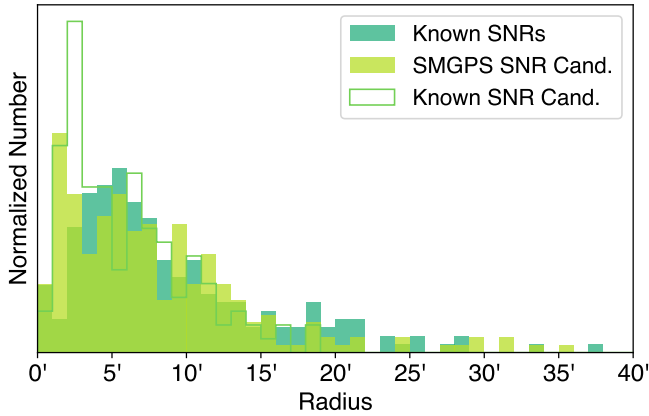


Fig. 9: Angular radius distributions for and known SNRs (red, from both the G22 and SNRCat samples) SNRs, SMGPS SNR candidates (light green filled), and previously-known SNR candidates (green open). Only sources detected in SMGPS images are shown.

- Kaplan, D. L., Kulkarni, S. R., Frail, D. A., & van Kerkwijk, M. H. 2002, *ApJ*, 566, 378
- Li, Z., Wheeler, J. C., Bash, F. N., & Jefferys, W. H. 1991, *ApJ*, 378, 93
- Mauch, T., Cotton, W., Condon, J., & et al. 2020, *ApJ*, 888, 61
- Maxted, N. I., Filipović, M. D., Hurley-Walker, N., et al. 2019, *ApJ*, 885, 129
- Ostriker, E. C., McKee, C. F., & Leroy, A. K. 2010, *ApJ*, 721, 975
- Ostriker, E. C. & Shetty, R. 2011, *ApJ*, 731, 41
- Padoan, P., Pan, L., Haugbølle, T., & Nordlund, Å. 2016, *ApJ*, 822, 11
- Pinheiro Gonçalves, D., Noriega-Crespo, A., Paladini, R., Martin, P. G., & Carey, S. J. 2011, *AJ*, 142, 47
- Ranasinghe, S. & Leahy, D. 2022, *arXiv e-prints*, arXiv:2209.04570
- Reach, W. T., Rho, J., Tappe, A., et al. 2006, *AJ*, 131, 1479
- Sidorin, V., Douglas, K. A., Palouš, J., Wünsch, R., & Ehlerová, S. 2014, *A&A*, 565, A6
- Stil, J. M., Taylor, A. R., Dickey, J. M., et al. 2006, *AJ*, 132, 1158
- Supan, L., Castelletti, G., Peters, W. M., & Kassim, N. E. 2018, *A&A*, 616, A98
- Sushch, I., Oya, I., Schwanke, U., Johnston, S., & Dalton, M. L. 2017, *A&A*, 605, A115
- Tammann, G. A., Loeffler, W., & Schroeder, A. 1994, *ApJS*, 92, 487
- Trushkin, S. A. 2001, in *ESA Special Publication*, Vol. 459, *Exploring the Gamma-Ray Universe*, ed. A. Gimenez, V. Reglero, & C. Winkler, 109–111
- Voit, G. M. 1992, *MNRAS*, 258, 841
- Weiler, K. W. & Sramek, R. A. 1988, *ARA&A*, 26, 295
- Whiteoak, J. B. Z. & Green, A. J. 1996, *A&AS*, 118, 329
- Wright, E. L., Eisenhardt, P. R. M., Mainzer, A. K., et al. 2010, *AJ*, 140, 1868